SLAC-PUB-13940

The Spectrum of the Isotropic Diffuse Gamma-Ray Emission Derived From First-Year Fermi Large Area Telescope Data

A. A. Abdo,[1,2] M. Ackermann,[3,*] M. Ajello,[3] W. B. Atwood,[4] L. Baldini,[5] J. Ballet,[6] G. Barbiellini,[7,8] D. Bastieri,[9,10] B. M. Baughman,[11] K. Bechtol,[3] R. Bellazzini,[5] B. Berenji,[3] R. D. Blandford,[3] E. D. Bloom,[3] E. Bonamente,[12,13] A. W. Borgland,[3] J. Bregeon,[5] A. Brez,[5] M. Brigida,[14,15] P. Bruel,[16] T. H. Burnett,[17] S. Buson,[10] G. A. Caliandro,[18] R. A. Cameron,[3] P. A. Caraveo,[19] J. M. Casandjian,[6] E. Cavazzuti,[20] C. Cecchi,[12,13] Ö. Çelik,[21,22,23] E. Charles,[3] A. Chekhtman,[1,24] C. C. Cheung,[1,2] J. Chiang,[3] S. Ciprini,[13] R. Claus,[3] J. Cohen-Tanugi,[25] L. R. Cominsky,[26] J. Conrad,[27,28,29] S. Cutini,[20] C. D. Dermer,[1] A. de Angelis,[30] F. de Palma,[14,15] S. W. Digel,[3] G. Di Bernardo,[5] E. do Couto e Silva,[3] P. S. Drell,[3] A. Drlica-Wagner,[3] R. Dubois,[3] D. Dumora,[31,32] C. Farnier,[25] C. Favuzzi,[14,15] S. J. Fegan,[16] W. B. Focke,[3] P. Fortin,[16] M. Frailis,[30] Y. Fukazawa,[33] S. Funk,[3] P. Fusco,[14,15] D. Gaggero,[5] F. Gargano,[15] D. Gasparrini,[20] N. Gehrels,[21,34,35] S. Germani,[12,13] B. Giebels,[16] N. Giglietto,[14,15] P. Giommi,[20] F. Giordano,[14,15] T. Glanzman,[3] G. Godfrey,[3] I. A. Grenier,[6] M.-H. Grondin,[31,32] J. E. Grove,[1] L. Guillemot,[36] S. Guiriec,[37] M. Gustafsson,[10,9] Y. Hanabata,[33] A. K. Harding,[21] M. Hayashida,[3] R. E. Hughes,[11] R. Itoh,[33] M. S. Jackson,[28,38] G. Jóhannesson,[3] A. S. Johnson,[3] R. P. Johnson,[4] T. J. Johnson,[21,35] W. N. Johnson,[1] T. Kamae,[3] H. Katagiri,[33] J. Kataoka,[39] N. Kawai,[40,41] M. Kerr,[17] J. Knödlseder,[42] M. L. Kocian,[3] F. Kuehn,[11] M. Kuss,[5] J. Lande,[3] L. Latronico,[5] M. Lemoine-Goumard,[31,32] F. Longo,[7,8] F. Loparco,[14,15] B. Lott,[31,32] M. N. Lovellette,[1] P. Lubrano,[12,13] G. M. Madejski,[3] A. Makeev,[1,24] M. N. Mazziotta,[15] W. McConville,[21,35] J. E. McEnery,[21,35] C. Meurer,[27,28] P. F. Michelson,[3] W. Mitthumsiri,[3] T. Mizuno,[33] A. A. Moiseev,[22,35] C. Monte,[14,15] M. E. Monzani,[3] A. Morselli,[43] I. V. Moskalenko,[3] S. Murgia,[3] P. L. Nolan,[3] J. P. Norris,[44] E. Nuss,[25] T. Ohsugi,[33] N. Omodei,[5] E. Orlando,[45] J. F. Ormes,[44] D. Paneque,[3] J. H. Panetta,[3] D. Parent,[31,32] V. Pelassa,[25] M. Pepe,[12,13] M. Pesce-Rollins,[5] F. Piron,[25] T. A. Porter,[4,†] S. Rainò,[14,15] R. Rando,[9,10] M. Razzano,[5] A. Reimer,[46,3] O. Reimer,[46,3] T. Reposeur,[31,32] S. Ritz,[4] L. S. Rochester,[3] A. Y. Rodriguez,[18] M. Roth,[17] F. Ryde,[38,28] H. F.-W. Sadrozinski,[4] D. Sanchez,[16] A. Sander,[11] P. M. Saz Parkinson,[4] J. D. Scargle,[47] A. Sellerholm,[27,28,‡] C. Sgrò,[5] M. S. Shaw,[3] E. J. Siskind,[48] D. A. Smith,[31,32] P. D. Smith,[11] G. Spandre,[5] P. Spinelli,[14,15] J.-L. Starck,[6] M. S. Strickman,[1] A. W. Strong,[45] D. J. Suson,[49] H. Tajima,[3] H. Takahashi,[33] T. Takahashi,[50] T. Tanaka,[3] J. B. Thayer,[3] J. G. Thayer,[3] D. J. Thompson,[21] L. Tibaldo,[9,10,6] D. F. Torres,[51,18] G. Tosti,[12,13] A. Tramacere,[3,52] Y. Uchiyama,[3] T. L. Usher,[3] V. Vasileiou,[22,23] N. Vilchez,[42] V. Vitale,[43,53] A. P. Waite,[3] P. Wang,[3] B. L. Winer,[11] K. S. Wood,[1] T. Ylinen,[38,54,28] and M. Ziegler[4]

[1] *Space Science Division, Naval Research Laboratory, Washington, DC 20375, USA*
[2] *National Research Council Research Associate, National Academy of Sciences, Washington, DC 20001, USA*
[3] *W. W. Hansen Experimental Physics Laboratory, Kavli Institute for Particle Astrophysics and Cosmology, Department of Physics and SLAC National Accelerator Laboratory, Stanford University, Stanford, CA 94305, USA*
[4] *Santa Cruz Institute for Particle Physics, Department of Physics and Department of Astronomy and Astrophysics, University of California at Santa Cruz, Santa Cruz, CA 95064, USA*
[5] *Istituto Nazionale di Fisica Nucleare, Sezione di Pisa, I-56127 Pisa, Italy*
[6] *Laboratoire AIM, CEA-IRFU/CNRS/Université Paris Diderot, Service d'Astrophysique, CEA Saclay, 91191 Gif sur Yvette, France*
[7] *Istituto Nazionale di Fisica Nucleare, Sezione di Trieste, I-34127 Trieste, Italy*
[8] *Dipartimento di Fisica, Università di Trieste, I-34127 Trieste, Italy*
[9] *Istituto Nazionale di Fisica Nucleare, Sezione di Padova, I-35131 Padova, Italy*
[10] *Dipartimento di Fisica "G. Galilei", Università di Padova, I-35131 Padova, Italy*
[11] *Department of Physics, Center for Cosmology and Astro-Particle Physics, The Ohio State University, Columbus, OH 43210, USA*
[12] *Istituto Nazionale di Fisica Nucleare, Sezione di Perugia, I-06123 Perugia, Italy*
[13] *Dipartimento di Fisica, Università degli Studi di Perugia, I-06123 Perugia, Italy*
[14] *Dipartimento di Fisica "M. Merlin" dell'Università e del Politecnico di Bari, I-70126 Bari, Italy*
[15] *Istituto Nazionale di Fisica Nucleare, Sezione di Bari, 70126 Bari, Italy*
[16] *Laboratoire Leprince-Ringuet, École polytechnique, CNRS/IN2P3, Palaiseau, France*
[17] *Department of Physics, University of Washington, Seattle, WA 98195-1560, USA*
[18] *Institut de Ciencies de l'Espai (IEEC-CSIC), Campus UAB, 08193 Barcelona, Spain*
[19] *INAF-Istituto di Astrofisica Spaziale e Fisica Cosmica, I-20133 Milano, Italy*
[20] *Agenzia Spaziale Italiana (ASI) Science Data Center, I-00044 Frascati (Roma), Italy*
[21] *NASA Goddard Space Flight Center, Greenbelt, MD 20771, USA*
[22] *Center for Research and Exploration in Space Science and Technology (CRESST) and NASA Goddard Space Flight Center, Greenbelt, MD 20771, USA*

Work supported in part by US Department of Energy contract DE-AC02-76SF00515.

[23]Department of Physics and Center for Space Sciences and Technology, University of Maryland Baltimore County, Baltimore, MD 21250, USA
[24]George Mason University, Fairfax, VA 22030, USA
[25]Laboratoire de Physique Théorique et Astroparticules, Université Montpellier 2, CNRS/IN2P3, Montpellier, France
[26]Department of Physics and Astronomy, Sonoma State University, Rohnert Park, CA 94928-3609, USA
[27]Department of Physics, Stockholm University, AlbaNova, SE-106 91 Stockholm, Sweden
[28]The Oskar Klein Centre for Cosmoparticle Physics, AlbaNova, SE-106 91 Stockholm, Sweden
[29]Royal Swedish Academy of Sciences Research Fellow, funded by a grant from the K. A. Wallenberg Foundation
[30]Dipartimento di Fisica, Università di Udine and Istituto Nazionale di Fisica Nucleare, Sezione di Trieste, Gruppo Collegato di Udine, I-33100 Udine, Italy
[31]Université de Bordeaux, Centre d'Études Nucléaires Bordeaux Gradignan, UMR 5797, Gradignan, 33175, France
[32]CNRS/IN2P3, Centre d'Études Nucléaires Bordeaux Gradignan, UMR 5797, Gradignan, 33175, France
[33]Department of Physical Sciences, Hiroshima University, Higashi-Hiroshima, Hiroshima 739-8526, Japan
[34]Department of Astronomy and Astrophysics, Pennsylvania State University, University Park, PA 16802, USA
[35]Department of Physics and Department of Astronomy, University of Maryland, College Park, MD 20742, USA
[36]Max-Planck-Institut für Radioastronomie, Auf dem Hügel 69, 53121 Bonn, Germany
[37]Center for Space Plasma and Aeronomic Research (CSPAR), University of Alabama in Huntsville, Huntsville, AL 35899, USA
[38]Department of Physics, Royal Institute of Technology (KTH), AlbaNova, SE-106 91 Stockholm, Sweden
[39]Waseda University, 1-104 Totsukamachi, Shinjuku-ku, Tokyo, 169-8050, Japan
[40]Department of Physics, Tokyo Institute of Technology, Meguro City, Tokyo 152-8551, Japan
[41]Cosmic Radiation Laboratory, Institute of Physical and Chemical Research (RIKEN), Wako, Saitama 351-0198, Japan
[42]Centre d'Étude Spatiale des Rayonnements, CNRS/UPS, BP 44346, F-30128 Toulouse Cedex 4, France
[43]Istituto Nazionale di Fisica Nucleare, Sezione di Roma "Tor Vergata", I-00133 Roma, Italy
[44]Department of Physics and Astronomy, University of Denver, Denver, CO 80208, USA
[45]Max-Planck Institut für extraterrestrische Physik, 85748 Garching, Germany
[46]Institut für Astro- und Teilchenphysik and Institut für Theoretische Physik, Leopold-Franzens-Universität Innsbruck, A-6020 Innsbruck, Austria
[47]Space Sciences Division, NASA Ames Research Center, Moffett Field, CA 94035-1000, USA
[48]NYCB Real-Time Computing Inc., Lattingtown, NY 11560-1025, USA
[49]Department of Chemistry and Physics, Purdue University Calumet, Hammond, IN 46323-2094, USA
[50]Institute of Space and Astronautical Science, JAXA, 3-1-1 Yoshinodai, Sagamihara, Kanagawa 229-8510, Japan
[51]Institució Catalana de Recerca i Estudis Avançats (ICREA), Barcelona, Spain
[52]Consorzio Interuniversitario per la Fisica Spaziale (CIFS), I-10133 Torino, Italy
[53]Dipartimento di Fisica, Università di Roma "Tor Vergata", I-00133 Roma, Italy
[54]School of Pure and Applied Natural Sciences, University of Kalmar, SE-391 82 Kalmar, Sweden

(Dated: February 18, 2010)

We report on the first Fermi Large Area Telescope (LAT) measurements of the so-called "extragalactic" diffuse γ-ray emission (EGB). This component of the diffuse γ-ray emission is generally considered to have an isotropic or nearly isotropic distribution on the sky with diverse contributions discussed in the literature. The derivation of the EGB is based on detailed modelling of the bright foreground diffuse Galactic γ-ray emission (DGE), the detected LAT sources and the solar γ-ray emission. We find the spectrum of the EGB is consistent with a power law with differential spectral index $\gamma = 2.41 \pm 0.05$ and intensity, $I(> 100\,\mathrm{MeV}) = (1.03 \pm 0.17) \times 10^{-5}$ cm^{-2} s^{-1} sr^{-1}, where the error is systematics dominated. Our EGB spectrum is featureless, less intense, and softer than that derived from EGRET data.

PACS numbers: 95.30.Cq,95.55.Ka,95.85.Pw,96.50.sb,98.70.Sa

Introduction: The high-energy diffuse γ-ray emission is dominated by γ-rays produced by cosmic rays (CR) interacting with the Galactic interstellar gas and radiation fields, the so-called diffuse Galactic emission (DGE). A much fainter component, commonly designated as "extragalactic γ-ray background" (EGB), was first detected against the bright DGE foreground by the *SAS-2* satellite [1] and later confirmed by analysis of the EGRET data [2]. The EGB by definition has an isotropic sky distribution and is considered by many to be the superposition of contributions from unresolved extragalactic sources including active galactic nuclei, starburst galaxies and γ-ray bursts ([3] and references therein) and truly-diffuse emission processes. These diffuse processes include the possible signatures of large-scale structure formation [4], emission produced by the interactions of

ultra-high-energy CRs with relic photons [5], the annihilation or decay of dark matter, and many other processes (e.g., [3] and references therein). However, the diffuse γ-ray emission from inverse Compton (IC) scattering by an extended Galactic halo of CR electrons could also be attributed to such a component if the size of the halo is large enough (i.e., $\sim$ 25 kpc) [6]. In addition, γ-ray emission from CRs interacting in populations of small solar system bodies [7] and the all-sky contribution of IC scattering of solar photons with local CRs can provide contributions [8–10]. Hence, an extragalactic origin for such a component is not clear, even though we will use the abbreviation 'EGB' throughout this paper.

In this paper, we present analysis and first results for the EGB derived from the Fermi Large Area Telescope (LAT) [11] data. Our analysis uses data from the initial 10 months of the science phase of the mission. Essential to this study is an event-level data selection with a higher level of background rejection than the standard LAT data selections, and improvements to the instrument simulation. These have been made following extensive on-orbit studies of the LAT performance and of charged particle backgrounds. Together, these improvements over the pre-launch modelling and background rejection allow a robust derivation of the spectrum of the EGB that is not possible with the standard low-background event selection.

Data selection: The LAT is a pair-conversion telescope with a precision tracker and segmented calorimeter, each consisting of a 4×4 array of 16 modules, a segmented anti-coincidence detector (ACD) that covers the tracker array, and a programmable trigger and data acquisition system. Details of the on-board and ground data processing are given in [11].

The LAT ground processing makes use of the pre-launch background rejection scheme described in [11]. The standard low-background event selection resulting from this multivariate analysis, termed "diffuse" class, has a Monte Carlo predicted background rate of ~ 0.1 Hz when integrated over the full instrument acceptance $>$ 100 MeV. On-orbit investigations of the residual background of misclassified particles in the diffuse event selection indicated a higher level than predicted from pre-launch modelling. To reduce the residual particle background further, we developed an event selection comprised of the following four criteria in addition to the standard diffuse event classification: 1) events are required to have a multivariate-analysis assigned γ-ray probability that is higher than the standard diffuse selection, with the required probability an increasing function with energy instead of a constant value as for diffuse class events; 2) the distance of extrapolated reconstructed particle tracks from the corners of the ACD must be higher than a set minimum value to remove particles that enter the LAT in a region where the ACD has a lower than average efficiency; 3) the average charge deposit in the silicon layers of the tracker is required to be small; 4) the reconstructed transverse shower size of events in the calorimeter is within a size range expected for electromagnetic showers. The first two criteria assist in reducing the overall level of CR background. The second two criteria provide an additional veto against hadronic showers and heavy ions that leak through the standard diffuse event classification. In addition to these analysis cuts the particle background modelling has been updated to be closer to the observed on-orbit charged particle rates. Furthermore, the instrument simulation now takes into account pile-up and accidental coincidence effects in the detector subsystems that were not considered in the definition of the pre-launch instrument response functions (IRFs) [12].

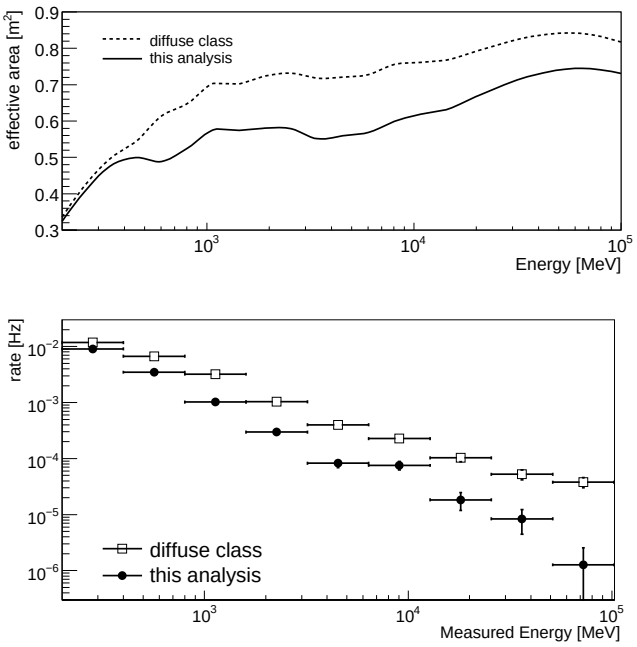

FIG. 1: Comparison of (a) LAT on-axis effective area and (b) orbit-averaged CR background rate integrated over the FOV between the enhanced low-background event selection and the standard "diffuse" event selection.

Figure 1a shows the on-axis effective area (A_{eff}) for our enhanced low-background and standard diffuse selections, respectively. The A_{eff} for the enhanced selection is reduced for energies $>$ 300 MeV with a peak value ~ 0.74 m^2 compared to ~ 0.84 m^2 for diffuse class events. The A_{eff} systematic uncertainties for our enhanced low-background selection are of the same magnitude as those for the diffuse class events, evaluated by comparing the efficiencies of analysis cuts for data and simulation of observations of Vela: 10% below 100 MeV, decreasing to 5% at 560 MeV, and increasing to 20% at 10 GeV and above. Figure 1b shows the orbit-averaged residual background rate of our enhanced low-background and standard diffuse selection, respectively, determined from our

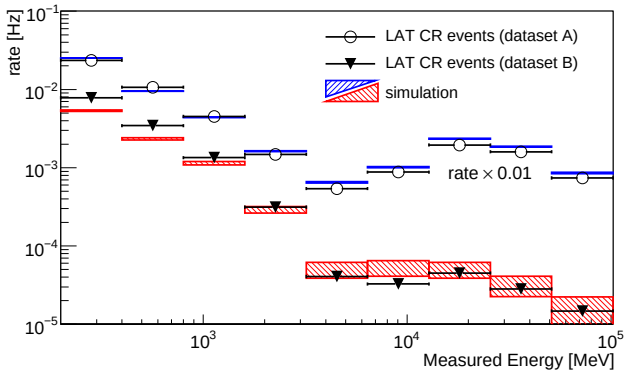

FIG. 2: Comparison of expected and measured orbit-averaged event rates for two CR dominated data samples.

improved simulation. With our enhanced event selection, the predicted background rejection is improved by a factor 1.3–10.

We estimate the uncertainty of the residual CR background in our simulation by comparing two CR background dominated LAT data samples to the predictions. The first data sample (A) contains all events passing the on-board filters, corresponding to a minimal background rejection level. The second data sample (B) contains events that pass the "source" classification in the standard analysis [11] but fail to pass the more stringent diffuse selection. This second sample corresponds to a very high level of background rejection but is still dominated by charged particles compared to the standard diffuse selection, particularly at intermediate and high Galactic latitudes. These particles are from the extreme tails of the CR distributions that are difficult to reject. To both samples we apply the selection cuts 3) and 4), described above, to remove the heavy ion and hadronic shower backgrounds observed on-orbit that are not modeled with sufficient accuracy in the simulation. In addition, to reduce the γ-ray fraction in both samples only events from Galactic latitudes $|b| \geq 45^\circ$ are used. The remaining γ-ray "contamination" is negligible for sample A due to the overwhelming CR rate. For sample B, the contamination is less than 10% above 1 GeV, but is almost 30% at 200 MeV, even at high Galactic latitudes. To remove this γ-ray contamination from sample B we use the intensity maps from our fits to the data (see below), combined with the IRFs corresponding to sample B, to determine the expected γ-ray rate. This is subtracted from the observed rate of sample B events.

Figure 2 compares the orbit-averaged event rates measured by the LAT and predicted by our simulation for datasets A and B. At the minimal background rejection level represented by sample A we find agreement within $\pm$ 20%. This shows that the bulk of the remaining CR background is well described by the simulation after removing the particular class of heavy ion and hadronic shower events mentioned above. For sample B, the agreement is within $+50\%/-30\%$, indicating the uncertainty in the description of the extreme tails of the CR distributions. As these tails are responsible for the limiting background in the present analysis, we adopt the results for sample B as representative of the uncertainty on the expected residual CR background.

Analysis: We use data taken in the nominal "scanning" mode from the commencement of scientific operations in mid-August 2008 to mid-June 2009. The data were prepared using the LAT Science Tools package, which is available from the Fermi Science Support Center[1]. Events satisfying our enhanced low-background event selection, coming from zenith angles $< 100^\circ$ (to greatly reduce the contribution by Earth albedo γ-rays) and incidence angles within 65° of the LAT z-axis (the LAT field-of-view) were used. This leaves 19 Ms of total observation time in the data set. The energy-dependent exposure was calculated using the IRFs corresponding to our enhanced low-background event selection described above.

The photon counts and exposure were further processed using the *GaDGET* package, part of a suite of tools we have developed to analyse the DGE [13]. Gamma-ray skymaps were generated using a HEALPix [14] isopixelisation scheme at order 6 with 9 independent energy bins from 200 MeV to 102 GeV with *GaDGET* used to simultaneously fit a DGE model, solar γ-ray emission, and sources (described below) to the resulting skymaps. We only consider the Galactic latitude range $|b| > 10^\circ$ in this analysis where the DGE is more than an order of magnitude weaker than in the Galactic plane.

The model used for the large-scale DGE is based on the GALPROP code[2]. Recent improvements include use of the formalism and corresponding code for pion production in *pp*-interactions by [15, 16], a complete recalculation of the ISRF [17], updated HI and H_2 gas maps, including corrections to the total gas column density derived from dust reddening maps [18] an improved line-of-sight integration routine, and the addition of information from our ongoing studies of the DGE with the LAT [19, 20]. Cosmic-ray intensities and spectra are calculated using a diffusive reacceleration CR transport model for a nominal halo size of 4 kpc, with a rigidity dependent diffusion coefficient that is consistent with available CR data for the B/C and ^{10}Be/^{9}Be ratios, respectively. We also consider bounding halo sizes 2 kpc and 10 kpc, with corresponding self-consistently derived diffusion coefficients, since the size of the CR halo is one of the principal uncertainties in the DGE foreground. The injection spectra for CR protons and primary electrons are cho-

[1] http://fermi.gsfc.nasa.gov/ssc/
[2] http://galprop.stanford.edu, model id 77XvMM7A.

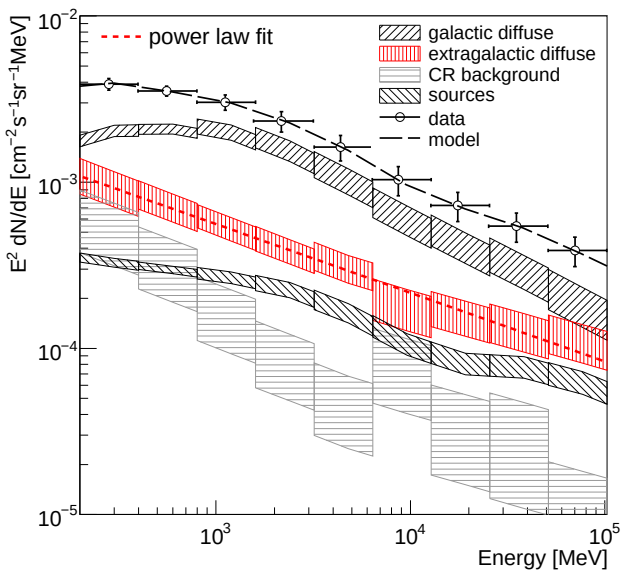

FIG. 3: LAT measured γ-ray intensity with fit results for $|b| \geq 10^\circ$ including statistical and systematic errors. Fit results by component are given in Table I. Note LAT data are dominated by systematic uncertainties for the energy range shown in the figure.

sen to reproduce after propagation the locally measured spectra, including the recently reported Fermi LAT CR electron spectrum [21]. Gamma-ray emissivities are calculated using the propagated CR spectra and intensities folded with the appropriate target distributions included in the GALPROP code: HI, H_2, and HII gas distributions for π^0-decay and bremsstrahlung, and the ISRF for IC scattering. Gamma-ray intensity skymaps are obtained by direct line-of-sight integration of the calculated γ-ray emissivities.

For the dominant high latitude components, bremssstrahlung and π^0-decay emission from HI and HII in the local Galaxy ($7.5\,\mathrm{kpc} < R < 9.5\,\mathrm{kpc}$) and IC emission, the intensities are fit to the LAT data via scale factors. We use the GALPROP skymaps as templates with the component normalisations per energy bin as fit parameters. The sub-dominant high-latitude DGE components, bremsstrahlung and π^0-decay from H_2, as well as HI and HII outside the local region defined above, are taken from GALPROP predictions and do not vary in the fit. All sources with test statistic above 200 (i.e., larger than $\sim 14\sigma$) found in the internal LAT 9-month source list are included with the flux per energy band per source as a fit parameter. Weaker sources are included with fluxes derived from the LAT catalogue analysis. In addition templates for the intensity of the γ-ray emission from CRs interacting in the solar disk and radiation field [8–10] that take into account the relative exposure as the Sun transits the celestial sphere are included with their normalisations as fit parameters.

Results: Figure 3 shows the γ-ray intensity measured by the LAT and the fit results for the Galactic latitude range $|b| \geq 10^\circ$. Table I summarises the numerical values and uncertainties, including the intensity values for the individually fitted DGE components that are not distinguished in figure 3 for clarity. The residual intensity obtained after fitting the DGE model components, solar emission, and sources is the sum of CR background and EGB. The simulation is used to estimate the CR background and uncertainty, as described earlier. The CR background is isotropic when averaged over the data taking period in this paper and is subtracted to obtain the EGB intensity. Additional figures for different latitude bands and regions of the sky can be found online [22].

Our formal uncertainty on the EGB comes from the fit using the nominal model. However, the RMS of the residual count fraction between LAT data and our model for energies above 200 MeV is 8.2%, when averaged over regions of 13.4 deg^2 to ensure sufficient statistics. This is larger than the 3.3% value expected solely from statistical fluctuations. We also see correlation of the residual count fraction with structures in the DGE model skymaps. This suggests a limitation in the accuracy of the description of the DGE model. We investigated the uncertainty on the EGB flux related to the DGE components by varying the relevant parameters in the model and re-evaluating the fits for $|b| > 10^\circ$. At high latitudes, the model parameters principally affecting the DGE are: the change of the IC emission with different halo sizes and the calculation of the IC emission using the anisotropic/isotropic formalism [23] (IC + halo in Table I), variations of the CR source distribution and X_{CO} gradient (CR propagation model), and how assumptions used to derive HI column densities from radio data and dust reddening measurements affect the distribution of HI in the local region (HI column density). To quantify the uncertainty connected to the residual count fraction, we used the nominal model and examined the variation of the derived EGB when different subregions of the $|b| > 10^\circ$ sky are fitted (Subregions of $|b| > 10^\circ$ sky). No single component dominates the uncertainties shown in the lower half of Table I. We caution that the uncertainties for the model components cannot be assumed to be independent. Hence, there is no simple relationship between the combination of individual components and the total formal uncertainty.

The large statistics allow sub-samples of the total data set to be used as a cross check. We repeated our analysis for events passing our enhanced selection with 1) different onboard trigger rates and 2) conversions in the thin or thick sections of the tracker [11]. The first sub-sample ensures that we have properly estimated the residual CR background, while the second checks that the small fraction of misreconstructed Earth albedo events that enter the LAT in the back section do not affect the result.

TABLE I: Fit results and uncertainties for the EGB and other components for $|b| \geq 10^\circ$.

	Intensity integrated over energy band ($\mathrm{cm^{-2}\ s^{-1}\ sr^{-1}}$)								
Energy in GeV	0.2–0.4	0.4–0.8	0.8–1.6	1.6–3.2	3.2–6.4	6.4–12.8	12.8–25.6	25.6–51.2	51.2–102.4
Scale factor	$\times 10^{-6}$	$\times 10^{-7}$	$\times 10^{-7}$	$\times 10^{-8}$	$\times 10^{-8}$	$\times 10^{-9}$	$\times 10^{-9}$	$\times 10^{-9}$	$\times 10^{-10}$
EGB	2.4 ± 0.6	9.3 ± 1.8	3.5 ± 0.6	12.7 ± 2.1	5.0 ± 1.0	14.3 ± 4.0	6.3 ± 1.5	2.6 ± 0.7	11.1 ± 2.9
Galactic diffuse (fit)	4.9 ± 0.4	25.9 ± 1.8	12.6 ± 1.3	50.7 ± 7.2	17.0 ± 3.0	50.0 ± 10	17.1 ± 3.6	6.1 ± 1.4	19.1 ± 5.2
Galactic diffuse (model)	5.0	26.0	11.5	43.3	14.7	47.9	15.7	5.2	17.0
IC (fit)	1.5 ± 0.1	6.8 ± 0.5	3.5 ± 0.4	16.1 ± 2.3	6.6 ± 1.2	23.3 ± 4.9	9.3 ± 2.1	3.9 ± 1.0	10.6 ± 3.7
IC (model)	1.2	5.3	2.3	9.7	4.0	16.2	6.3	2.4	8.7
local HI (fit)	2.7 ± 0.2	15.4 ± 1.1	7.4 ± 0.8	28.3 ± 4.0	8.3 ± 1.5	20.6 ± 4.2	5.9 ± 1.2	1.6 ± 0.4	7.0 ± 2.2
local HI (model)	3.1	17.0	7.6	27.6	8.7	26.0	7.7	2.3	6.8
Sources	0.8 ± 0.1	3.8 ± 0.2	1.7 ± 0.1	7.2 ± 0.8	2.7 ± 0.4	9.0 ± 1.3	3.4 ± 0.5	1.5 ± 0.2	6.3 ± 1.0
CR background	1.4 ± 0.6	4.2 ± 1.7	1.0 ± 0.4	2.8 ± 1.2	0.8 ± 0.4	6.3 ± 3.0	1.4 ± 0.8	0.6 ± 0.4	0.9 ± 0.9
Solar	0.1 ± 0.01	0.4 ± 0.04	0.2 ± 0.02	1.0 ± 0.2	0.4 ± 0.2	1.7 ± 0.4	0.7 ± 1.6	0.1 ± 0.04	0.8 ± 0.5
LAT	9.6 ± 0.8	44.0 ± 3.0	18.8 ± 2.0	72.9 ± 10	25.3 ± 4.5	81.3 ± 16	28.3 ± 5.7	10.6 ± 2.1	37.9 ± 7.7
	Foreground modeling related uncertainty in $\mathrm{cm^{-2}\ s^{-1}\ sr^{-1}}$								
HI column density	$+0.1/-0.3$	$+0.1/-1.7$	$+0.1/-0.9$	$+0.1/-3.6$	$+0.1/-1.1$	$+0.1/-2.4$	$+0.1/-0.9$	$+0.1/-0.2$	$+0.1/-1.1$
IC + halo size	$+0.1/-0.2$	$+0.1/-0.8$	$+0.1/-0.5$	$+0.1/-1.8$	$+0.1/-0.5$	$+0.1/-0.7$	$+0.3/-0.3$	$+0.4/-0.1$	$+2.9/-0.5$
CR propagation model	$+0.1/-0.3$	$+0.1/-1.1$	$+0.1/-0.6$	$+0.1/-0.8$	$+0.1/-0.3$	$+0.1/-1.2$	$+1.4/-0.1$	$+0.4/-0.1$	$+3.0/-0.1$
Subregions of $\lvert b\rvert > 10^\circ$ sky	$+0.2/-0.3$	$+0.8/-1.5$	$+0.4/-0.9$	$+1.9/-2.1$	$+0.7/-0.5$	$+2.5/-1.9$	$+1.0/-1.5$	$+0.5/-0.3$	$+2.7/-0.9$

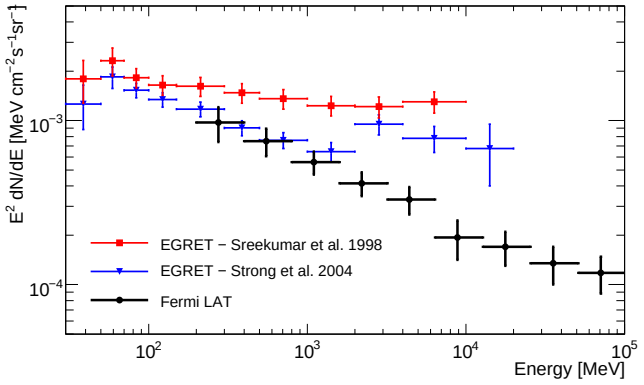

FIG. 4: EGB intensity derived in this work compared with EGRET-derived intensities taken from table 1 in [2] and table 3 in [24]. Our derived spectrum is compatible with a simple power-law with index $\gamma = 2.41 \pm 0.05$ and intensity $I(> 100\,\mathrm{MeV}) = (1.03 \pm 0.17) \times 10^{-5}$ $\mathrm{cm^{-2}\ s^{-1}\ sr^{-1}}$ where the uncertainties are systematics dominated.

The derived EGB spectrum for these sub-samples is completely consistent with that derived from the full data set using the same analysis procedure.

Finally, we note that our analysis also indicates a significant detection of the combined solar disk and extended solar IC emission. This finding will be explored in more detail in a separate study.

Discussion: Figure 4 shows the spectrum of the EGB above 200 MeV derived in the present analysis, and from EGRET data [2, 24]. Our intensity extrapolated to 100 MeV based on the power-law fit, $I(> 100\,\mathrm{MeV}) = (1.03 \pm 0.17) \times 10^{-5}$ $\mathrm{cm^{-2}\ s^{-1}\ sr^{-1}}$, is significantly lower than that obtained from EGRET data: $I_{\mathrm{EGRET}}(> 100\,\mathrm{MeV}) = (1.45 \pm 0.05) \times 10^{-5}$ $\mathrm{cm^{-2}\ s^{-1}\ sr^{-1}}$ [2]. Furthermore, our spectrum is compatible with a featureless power law with index $\gamma = 2.41 \pm 0.05$. This is significantly softer than the EGRET spectrum with index $\gamma_{\mathrm{EGRET}} = 2.13 \pm 0.03$ [2]. To check that the different spectra are not due to the instrumental point-source sensitivities, we adopt $F(> 100\,\mathrm{MeV}) = 10^{-7}$ $\mathrm{cm^{-2}\ s^{-1}}$, comparable to the average EGRET sensitivity, and attribute the flux of all detected LAT sources below this threshold to the EGB. We obtain an intensity $I_{res}(> 100\,\mathrm{MeV}) = (1.19 \pm 0.18) \times 10^{-5}$ $\mathrm{cm^{-2}\ s^{-1}\ sr^{-1}}$ and a spectrum compatible with a power-law with index $\gamma_{res} = 2.37 \pm 0.05$. Therefore, the discrepancy cannot be attributed to a lower threshold for resolving point sources. Our EGB intensity is comparable to that obtained in the EGRET re-analysis by [24] with an updated DGE model, $I_{\mathrm{SMR}}(> 100\,\mathrm{MeV}) = (1.11 \pm 0.1) \times 10^{-5}$ $\mathrm{cm^{-2}\ s^{-1}\ sr^{-1}}$. However, our EGB spectrum does not show the distinctive harder spectrum above $\gtrsim 1$ GeV and peak at ~ 3 GeV found in the same EGRET reanalysis. We note that the LAT-measured spectra are softer above $\gtrsim 1$ GeV than those measured by EGRET also for the DGE at intermediate latitudes [20] and for the Vela Pulsar [25].

Acknowledgements: The Fermi LAT Collaboration acknowledges support from a number of agencies and institutes for both development and the operation of the LAT as well as scientific data analysis. These include NASA and DOE in the United States, CEA/Irfu and IN2P3/CNRS in France, ASI and INFN in Italy, MEXT, KEK, and JAXA in Japan, and the K. A. Wallenberg Foundation, the Swedish Research Council and the National Space Board in Sweden. Additional support from INAF in Italy and CNES in France for science analysis during the operations phase is also gratefully acknowledged. GALPROP development is partially funded via NASA grant NNX09AC15G. Some of the results in this paper have been derived using the HEALPix [14] pack-

age.

* Electronic address: markusa@slac.stanford.edu
† Electronic address: tporter@scipp.ucsc.edu
‡ Electronic address: sellerholm@physto.se

[1] C. E. Fichtel, G. A. Simpson, and D. J. Thompson, Astrophys. J. **222**, 833 (1978).
[2] P. Sreekumar et al., Astrophys. J. **494**, 523 (1998).
[3] C. D. Dermer, AIP Conf. Proc. **921**, 122 (2007).
[4] A. Loeb and E. Waxman, Nature (London) **405**, 156 (2000).
[5] O. E. Kalashev, D. V. Semikoz, and G. Sigl, Phys. Rev. D **79**, 063005 (2009).
[6] U. Keshet, E. Waxman, and A. Loeb, Journal of Cosmology and Astro-Particle Physics **4**, 6 (2004).
[7] I. V. Moskalenko and T. A. Porter, Astrophys. J. Lett. **692**, L54 (2009).
[8] I. V. Moskalenko, T. A. Porter, and S. W. Digel, Astrophys. J. Lett. **652**, L65 (2006).
[9] E. Orlando and A. W. Strong, Astron. & Astrophys. **480**, 847 (2008).
[10] I. V. Moskalenko, T. A. Porter, and S. W. Digel, Astrophys. J. Lett. **664**, L143 (2007), erratum.
[11] W. B. Atwood et al., Astrophys. J. **697**, 1071 (2009).
[12] R. Rando et al., ArXiv e-prints (2009), 0907.0626.
[13] M. Ackermann et al., AIP Conf. Proc. **1085**, 763 (2009).
[14] Górski et al., Astrophys. J. **622**, 759 (2005).
[15] T. Kamae et al., Astrophys. J. **647**, 692 (2006).
[16] S. R. Kelner, F. A. Aharonian, and V. V. Bugayov, Phys. Rev. D **74**, 034018 (2006).
[17] T. A. Porter et al., Astrophys. J. **682**, 400 (2008).
[18] I. A. Grenier, J.-M. Casandjian, and R. Terrier, Science **307**, 1292 (2005).
[19] A. A. Abdo et al., Astrophys. J. **703**, 1249 (2009).
[20] A. A. Abdo et al., Phys. Rev. Lett. **103**, 251101 (2009).
[21] A. A. Abdo et al., Phys. Rev. Lett. **102**, 181101 (2009).
[22] See EPAPS Document xxx for additional figures. For more information on EPAPS, see http://www.aip.org/pubservs/epaps.html.
[23] I. V. Moskalenko and A. W. Strong, Astrophys. J. **528**, 357 (2000).
[24] A. W. Strong, I. V. Moskalenko, and O. Reimer, Astrophys. J. **613**, 956 (2004).
[25] A. A. Abdo et al., Astrophys. J. **696**, 1084 (2009).

THE SPECTRUM OF THE ISOTROPIC DIFFUSE GAMMA-RAY EMISSION DERIVED FROM FIRST-YEAR FERMI LARGE AREA TELESCOPE DATA. SUPPLEMENTARY ONLINE MATERIAL.

Abstract

Supplementary material concerning the analysis presented in "The Spectrum of the Isotropic Diffuse Gamma-Ray Emission Derived From First-Year Fermi Large Area Telescope Data" is presented here.

Galactic diffuse model

Figure 5 displays the individually fitted contributions to the galactic diffuse emission arising from inverse Compton emission and interaction of CRs with atomic hydrogen in the local Galaxy (7.5 kpc $\leq$ r $\leq$ 9.5 kpc) via bremsstrahlung and pion decay. These contributions are omitted in figure 3 of the published article for visual clarity, but numerically available in table 1. The intensity is averaged over galactic latitudes $|b| \geq 10°$. The cosmic-ray contamination is subtracted from the EGB component shown here. Its contribution can be found in figure 3 of the published article. The errors shown in the graphs are the quadratic sum of statistical and systematic errors due to uncertainties in the LAT effective area and CR background subtraction.

Comparisons for different sky regions

Figure 3 in the published article compares the modeled with the measured γ-ray intensity averaged over all galactic latitudes $|b| \geq 10°$. To illustrate the good agreement of the used γ-ray emission model, i.e. galactic diffuse emission, EGB, point sources and solar emission, over the whole fitted region, it is interesting to display this comparison for different sub-regions of the sky.

Figure 6 shows the intensities of different components in the model when averaged over independent Galactic latitude ranges covering low, mid and high galactic latitudes, $10° \leq |b| \leq 20°$, $20° \leq |b| \leq 60°$ and $|b| \geq 60°$. Figure 7 shows the intensities of different components in the model when averaged over different hemispheres. The hemispheres considered are centered at the North Galactic pole ($b \geq 0°$), the South Galactic pole ($b \leq 0°$), the Galactic center ($270° \leq l \leq 90°$) and anticenter ($90° \leq l \leq 270°$). Furthermore, Galactic latitudes $|b| < 10°$ are excluded from all hemispheres.

We emphasize that the intensities of the components shown in the figures are from the single gamma-ray emission model used in the analysis. In particular, the EGB component in each figure is identical because it is isotropic by construction and thus its average intensity does not vary across the sky. The accuracy of the model with respect to the different sub-regions of the sky shown can be judged by comparing the total predicted model intensity (black line in figure 6) to the measured gamma-ray intensities per energy band represented by the data points.

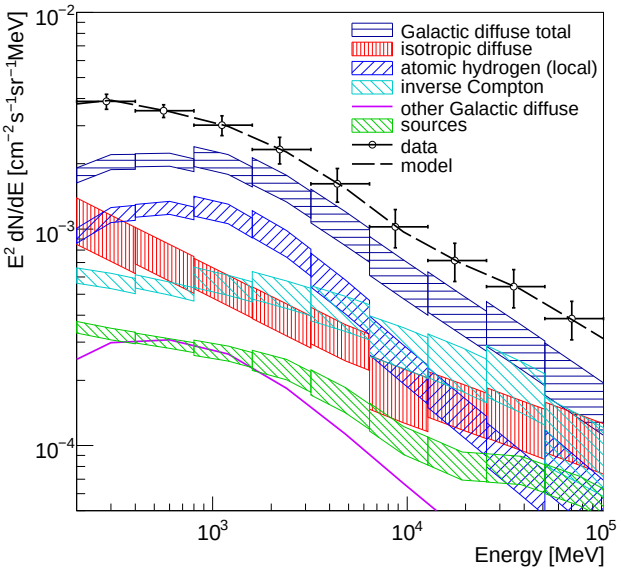

FIG. 5: LAT measured γ-ray intensity with fit results for $|b| \geq 10°$ including statistical and systematic errors. Independently fitted components of the galactic diffuse emission are shown individually. "Other Galactic diffuse" denotes the sum of the H_2 and non-local HI and HII contributions which are included using the model intensities (i.e., no fit). Note LAT data are dominated by systematic uncertainties for the energy range shown in the figure. Ths intensity of the solar emission considered in the model is below the range shown in the figure.

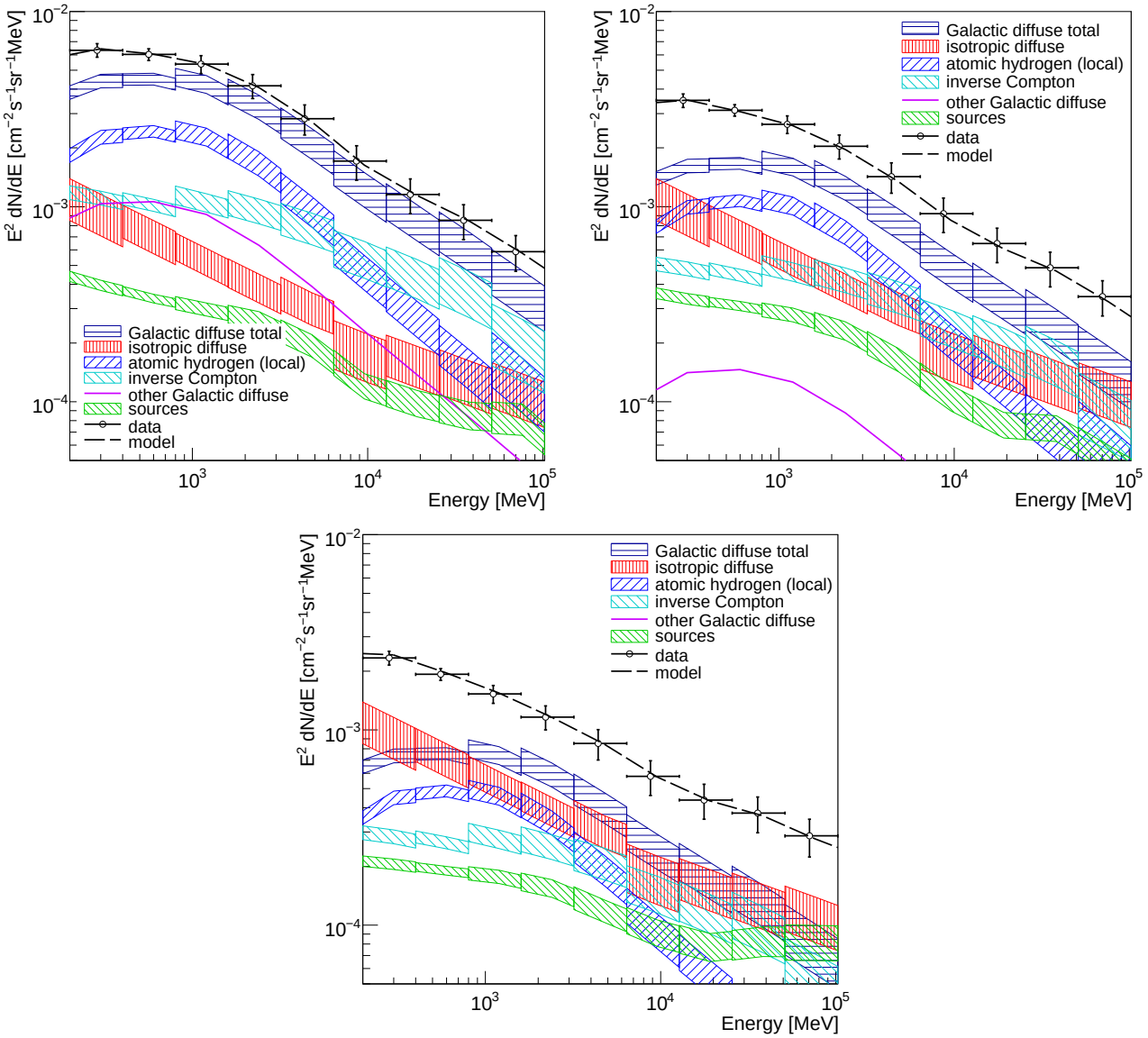

FIG. 6: LAT measured intensity compared to the γ-ray emission model used in the derivation of the EGB averaged over different ranges in Galactic latitude. The regions shown are $10^\circ \leq |b| \leq 20^\circ$ (upper left), $20^\circ \leq |b| \leq 60^\circ$ (upper right) and $|b| \geq 60^\circ$ (lower center). "Other Galactic diffuse" denotes the sum of the H_2 and non-local HI and HII contributions which are included using the model intensities (i.e., no fit). Errors include statistical and systematic errors. LAT data are dominated by systematic uncertainties for the energy range displayed in the figure.

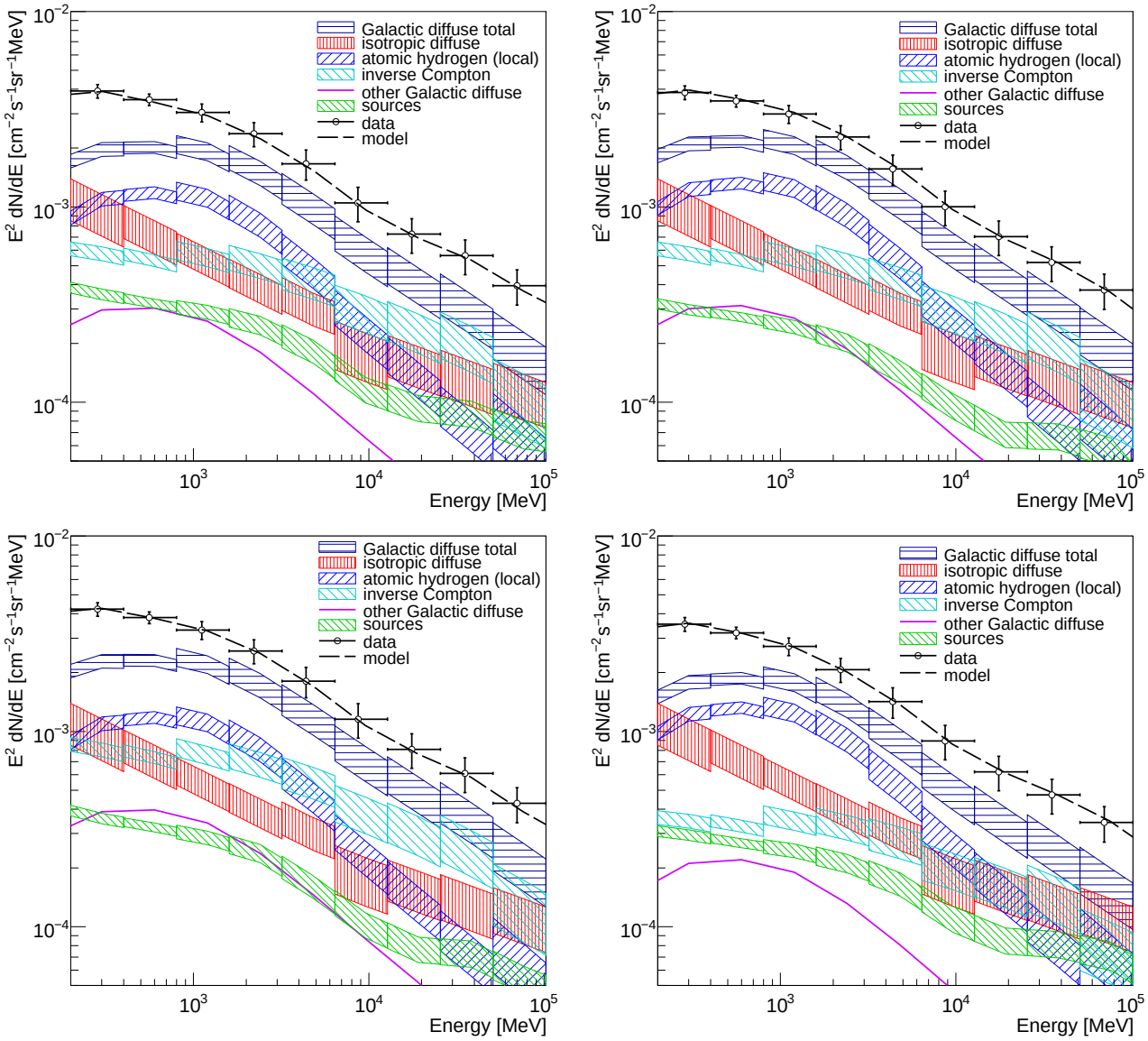

FIG. 7: LAT measured intensity compared to the γ-ray emission model used in the derivation of the EGB averaged over different hemispheres on the sky for Galactic latitudes $|b| \geq 10^{\circ}$. The hemispheres shown are centered at the North Galactic pole (upper left), the South Galactic pole (upper right), the Galactic center (lower left) and anti-center (lower right). "Other Galactic diffuse" denotes the sum of the H_2 and non-local HI and HII contributions which are included using the model intensities (i.e., no fit). Errors include statistical and systematic errors. LAT data are dominated by systematic uncertainties for the energy range displayed in the figure.